Progress In Electromagnetics Research B, Vol. 45, 117–146, 2012

ISOGEOMETRIC SHAPE OPTIMIZATION FOR ELECTROMAGNETIC SCATTERING PROBLEMS

D. M. Nguyen[1], A. Evgrafov[2, *], and J. Gravesen[2]

[1]Department of Applied Mathematics, SINTEF Information and Communication Technology, Forskningsveien 1, Oslo N-0373, Norway

[2]Department of Mathematics, Technical University of Denmark, Matematiktorvet 303B, Kgs. Lyngby DK-2800, Denmark

Abstract—We consider the benchmark problem of magnetic energy density enhancement in a small spatial region by varying the shape of two symmetric conducting scatterers. We view this problem as a prototype for a wide variety of geometric design problems in electromagnetic applications. Our approach for solving this problem is based on shape optimization and isogeometric analysis. One of the major difficulties we face to make these methods work together is the need to maintain a valid parametrization of the computational domain during the optimization. Our approach to generating a domain parametrization is based on minimizing a second order approximation to the Winslow functional in the vicinity of a reference parametrization. Furthermore, we enforce the validity of the parametrization by ensuring the non-negativity of the coefficients of a B-spline expansion of the Jacobian. The shape found by this approach outperforms earlier design computed using topology optimization by a factor of one billion.

1. INTRODUCTION

Shape optimization has been a subject of a great interest in the past decades, see for example [1–3], and the references therein. Such an interest is fuelled by many important and direct applications of shape optimization in various engineering disciplines, and the subject has seen many advances during these years. In this paper, we concentrate on utilizing shape optimization techniques to facilitate optimal design for electromagnetic (EM) scattering applications.

Received 13 September 2012, Accepted 16 October 2012, Scheduled 24 October 2012

* Corresponding author: Anton Evgrafov (A.Evgrafov@mat.dtu.dk).

Many shape optimization approaches continue to rely on polygonal grids inherited from the underlying numerical methods used for approximating partial differential equations (PDEs) governing a given physical system under consideration, Maxwell's equations in our case. This creates a disparity between a computer aided design (CAD)-like geometric representation of the shape, which is most often utilized for manufacturing purposes, and a polygonal representation utilized for the numerical computations [1, 4, 5]. Additionally, the need for automatic remeshing often imposes artificial limits on the admissible variations of shapes, in turn limiting the possible improvements of the performance, see for example [1, 6] and references therein for a discussion.

The arrival of isogeometric analysis (IGA) [7] provided the subject of shape optimization with a new direction of development. Potential benefits of shape optimization based on IGA have been indicated in the original paper [7], and have later been further explored in [6, 8–12]. In particular, complex shapes can be represented with relatively few variables using splines, thus allowing one to reduce the dimension of the shape optimization problem. Furthermore, since the IGA framework eliminates the disagreement between the CAD and the analysis representations, optimized designs can easily be exported to a CAD system for manufacturing [7, 13].

The issue of remeshing in traditional FEA is replaced by the reparametrization problem in IGA-based shape optimization. A robust and inexpensive method for reparametrizing the physical domain during the shape optimization is required. The need for such a reparametrization has been addressed in Nguyen et al. [6], and two linear methods have been proposed for this purpose. Unfortunately, linear methods can not in general treat large deviations from the initial geometrical configuration. In this paper, we utilize the observation that minima of Winslow functional [14] correspond to high quality (nearly-conformal) parametrizations [15]. However, solving an auxiliary non-convex mathematical programming problem at every shape optimization iteration is computationally too expensive. Therefore, we only do this occasionally in order to compute a reference parametrization. During regular iterations we work with quadratic optimization problems (whose optimality conditions are linear systems) based on a second order Taylor series expansion of the non-linear Winslow functional around the reference parametrization. To prevent self-intersection of the boundary of the domain, we formulate a set of easily computable sufficient conditions that guarantee non-self-intersecting boundaries without greatly restricting the family of available shapes.

In the situation where we are interested in the behaviour of the EM fields near the scatterers (near field models), shape optimization based on IGA is a very natural choice. It is well known, both theoretically and experimentally, that the fields are quite sensitive with respect to the precise location and the shape of the air-scatterer interface. Utilizing the same geometric representation for the analysis and manufacturing is an essential advantage in this case.

Systematic optimal design for EM applications has been performed previously utilizing techniques of topology optimization [16]. Within the framework of topology optimization (see, for example [17, 18]), also known as control in the coefficients or shape optimization through homogenization, one approaches the shape optimization problem from an entirely different angle. In the present case the geometry of the scatterer are encoded in the coefficients of Maxwell's equations, which remain valid both in the dielectric or air phase and inside the conducting scatterer. Interpolating between the two phases/values of the coefficients, one casts the shape optimization problem into a problem of finding the coefficients of Maxwell's equations assuming only two extreme values (dielectric/conductor phase), which maximize a given performance functional. However, computational complications arise owing to the fast variation of the EM fields near the interface ("the skindepth problem"). To resolve these complications, one needs either a computationally infeasibly fine mesh, or rather special numerical treatment, see [16]. The results obtained in [16] are shown in Fig. 1. Note that this way of representing the geometry yields a rough and imprecise boundary of the optimized shape, see Fig. 1(b). Nevertheless we use this result of topology optimization as a benchmark result for our IGA-based shape optimization algorithm.

At the frequencies, we are considering the skindepth is small compared to the thickness of the scatter so by maintaining an explicit representation of the interface during the optimization we can use the appropriate (transmission) boundary conditions. Additionally, we automatically maintain the regularity of the boundary by representing it with B-splines. Compared with the topology optimization result, we obtain a scatter configuration that performs by a factor of 10^9 better in terms of focusing the magnetic energy in the prescribed area. The same is true when compared with two standard scatter configurations, two circles and a "bowtie".

The paper is organized as follows. In Section 2, we state the mathematical model of the scattering problem and describe its numerical discretization using isogeometric analysis. In Section 3, we present the shape optimization problem of scatterer's geometry and outline the sensitivity analysis and the computational strategy

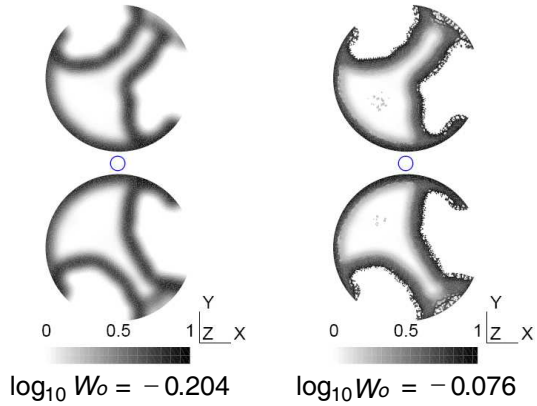

Figure 1. Two topology optimization results taken from Aage et al. [16]. W_o is proportional to the magnetic energy calculated in the small circular domain between the two scatterers.

for solving this problem. Numerical experiments are presented in Section 4. We conclude the discussion in Section 5. In Appendix A, we describe our method of approximating a circular arc with a spline curve, this is used several times in the paper.

2. THE PHYSICAL PROBLEM AND ITS DISCRETIZATION

In this section, we briefly describe the models used in the present work to simulate a 2D electromagnetic scattering problem.

2.1. The Electromagnetic Scattering Problem

We consider a two-dimensional EM TE_z model, that is, the situation when the z-component of the electric field's intensity vanishes. In particular, we look at a scattering problem in which a uniform plane wave with a frequency f travels through a linear and isotropic dielectric in the presence of conducting scatterers with high electric conductivity σ. The incident magnetic field intensity is given as $\mathbf{H}^i = (0, 0, H_z^i)$. We denote the relative complex permittivity and permeability of the dielectric by ε_{cr} and μ_r, and those of the scatterer by ε_{cr}^s and μ_r^s. Note that $\varepsilon_{cr}^s = \varepsilon_r^s - j\dfrac{\sigma}{\omega\varepsilon_0}$, where $j^2 = -1$ and $\omega = 2\pi f$. All EM fields in this paper are assumed to be time-harmonic with an $e^{j\omega t}$ time dependence.

The infinite domain outside the scatterers is truncated by an approximation to a circle with radius r_t, as shown in Fig. 2. At the truncation boundary we use the first order absorbing boundary condition [19], and the present frequencies we can use the impedance boundary condition at the scatters boundary [19]. The equations modeling such a problem, c.f. [19], are

$$\boldsymbol{\nabla} \cdot \left(\frac{1}{\varepsilon_{cr}} \boldsymbol{\nabla} H_z \right) + k_0^2 \mu_r H_z = 0 \qquad \text{in } \Omega, \tag{1a}$$

$$\frac{1}{\varepsilon_{cr}} \frac{\partial H_z}{\partial \mathbf{n}} - jk_0 \sqrt{\frac{\mu_r^{\mathrm{s}}}{\varepsilon_{cr}^{\mathrm{s}}}} H_z = 0 \qquad \text{on } \Gamma_s, \tag{1b}$$

$$\frac{\partial (H_z - H_z^i)}{\partial \mathbf{n}} + \left(jk_0 + \frac{1}{2r_t} \right) \left(H_z - H_z^i \right) = 0 \qquad \text{on } \Gamma_t, \tag{1c}$$

where $k_0 = 2\pi f \sqrt{\varepsilon_0 \mu_0}$, ε_0, and μ_0 are the wavenumber, the permittivity, and the permeability of free space, respectively, and $\mathbf{n}$ is the outward unit normal vector on $\Gamma_s \cup \Gamma_t$. Note that the equations entering (1) are invariant under simultaneous scaling of the frequency and size of the domain except for the frequency dependence of the complex permittivity of the scatterer.

A variational statement of (1) may be written as follows: find $H_z \in H^1(\Omega)$ (see [20]) such that for every $\phi \in H^1(\Omega)$ we have the

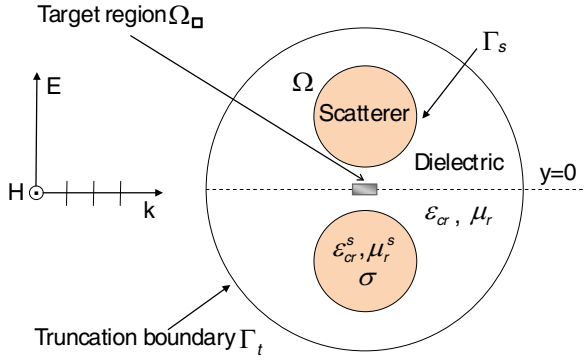

Figure 2. Model scattering problem considered in this work. Due to the symmetry, only the upper half of the truncated domain is modelled.

equality:

$$\int_\Omega \frac{1}{\varepsilon_{cr}} \boldsymbol{\nabla} H_z \cdot \boldsymbol{\nabla} \phi \, \mathrm{d}V - k_0^2 \int_\Omega \mu_r H_z \, \phi \, \mathrm{d}V$$

$$-jk_0 \int_{\Gamma_s} \sqrt{\frac{\mu_r^{\mathrm{s}}}{\varepsilon_{cr}^{\mathrm{s}}}} H_z \, \phi \, \mathrm{d}\Gamma + \left(jk_0 + \frac{1}{2r_t} \right) \int_{\Gamma_t} \frac{1}{\varepsilon_{cr}} H_z \, \phi \, \mathrm{d}\Gamma$$

$$= \int_{\Gamma_t} \frac{1}{\varepsilon_{cr}} \left(\frac{\partial H_z^i}{\partial \mathbf{n}} + \left(jk_0 + \frac{1}{2r_t} \right) H_z^i \right) \phi \, \mathrm{d}\Gamma. \tag{2}$$

We assume that the incident field is a plane wave propagating in the x-direction, that is $H_z^i = e^{-jk_0\sqrt{\varepsilon_{cr}\mu_{cr}}x}$, and consider two scatterers which are symmetric about the x-axis. As a result, H_z is also symmetric about the x-axis. Thus we can solve the problem in half of the domain augmented with the following boundary condition:

$$\frac{\partial H_z}{\partial y} = 0 \quad \text{if} \quad y = 0. \tag{3}$$

2.2. Fundamentals of Isogeometric Analysis

We discretize the physical problem (1) using isogeometric analysis, a modern numerical method for approximating PDEs [13]. Similarly to the standard FEA, the underlying principle of IGA is the use of the Galerkin method [21]. Thus we approximate the weak solution to a given boundary value problem associated with Maxwell's equations in a finite-dimensional space spanned by certain basis (shape) functions. In the present case, the basis functions are defined indirectly via a spline parametrization of the physical domain and bivariate tensor product B-splines in the parameter domain $]0,1[^2$.

2.2.1. B-splines

B-splines are piecewise polynomials of a certain degree p, typically differentiable up to the degree $p-1$, which are non-negative and compactly supported, see Fig. 3(a). They are completely defined by specifying certain parameter values, called *knots*, $\xi_1 \leq \ldots \leq \xi_{n+p+1}$, where polynomial pieces come together. More precisely, B-splines may be defined recursively as follows: for $i = 1, \ldots, n$ we put

$$N_i^0(\xi) = \begin{cases} 1 & \text{if} \quad \xi \in [\xi_i, \xi_{i+1}[, \\ 0 & \text{otherwise,} \end{cases}$$

$$N_i^p(\xi) = \frac{\xi - \xi_i}{\xi_{i+p} - \xi_i} N_i^{p-1}(\xi) + \frac{\xi_{i+p+1} - \xi}{\xi_{i+p+1} - \xi_{i+1}} N_{i+1}^{p-1}(\xi), \qquad p > 0.$$

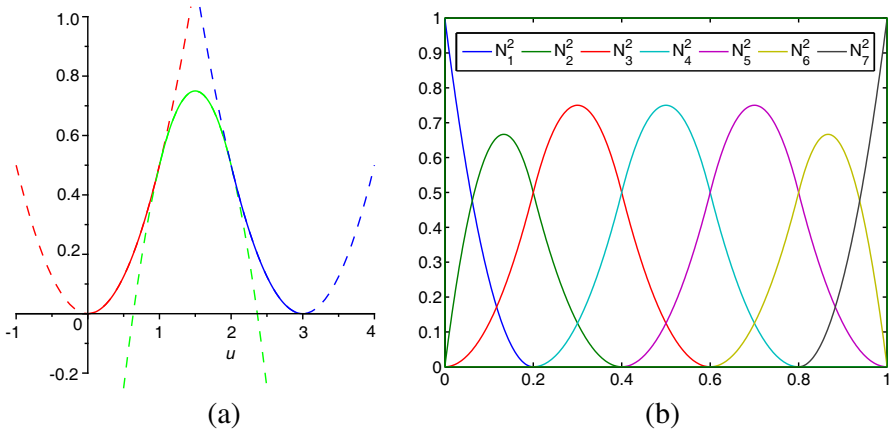

Figure 3. (a) A quadratic B-spline composed of polynomial "pieces" (shown in different colors). The alignments of the dashed-straight lines show that the B-spline is C^1-continuous at the knots. (b) Quadratic B-splines with the knot vector $\{0, 0, 0, 0.2, 0.4, 0.6, 0.8, 1, 1, 1\}$.

In the context of IGA, the *knot vector* $\boldsymbol{\Xi} = \{\xi_1, \ldots, \xi_{n+p+1}\}$ typically has its first and last knots set to 0 and 1, respectively, and repeated $p + 1$ times. That is, we have $\xi_1 = \ldots = \xi_{p+1} = 0$ and $\xi_{n+1} = \ldots = \xi_{n+p+1} = 1$, see Fig. 3(b). Such B-splines form a partition of unity on $[0, 1[$. Further properties of B-splines can be found in, e.g., [22, 23].

2.2.2. Basis Functions for IGA

Let us consider a simply connected domain $\Omega \subset \mathbb{R}^2$. A spline parametrization of Ω is a *bijective* map $\mathbf{F} :]0, 1[^2 \rightarrow \Omega$ of the form

$$\mathbf{F}(u, v) = \big(x(u, v), y(u, v)\big) = \sum_{i=1}^{\widehat{m}} \sum_{j=1}^{\widehat{n}} \widehat{\mathbf{d}}_{i,j} \widehat{M}_i^p(u) \widehat{N}_j^q(v), \qquad (4)$$

where $\widehat{M}_i^p$ and $\widehat{N}_i^q$ are B-splines of degree p and q with knot vectors $\widehat{\boldsymbol{\Xi}}_u$ and $\widehat{\boldsymbol{\Xi}}_v$, respectively. By composing the inverse $\mathbf{F}^{-1}$ with some basis functions on the parameter (reference) domain $]0, 1[^2$ we obtain basis functions defined on the physical domain Ω. We let $\widetilde{M}_i^{\widetilde{p}}$, $i = 1, \ldots, \widetilde{m}$ and $\widetilde{N}_j^{\widetilde{q}}$, $j = 1, \ldots, \widetilde{n}$ be B-splines of degree $\widetilde{p}$ and $\widetilde{q}$ (not necessary equal to p and q) with knot vector $\widetilde{\boldsymbol{\Xi}}_u$ and $\widetilde{\boldsymbol{\Xi}}_v$, respectively. The basis functions on the parameter domain are defined as the tensor product splines $\widetilde{R}_k^{\widetilde{p},\widetilde{q}}(u, v) = \widetilde{M}_i^{\widetilde{p}}(u) \widetilde{N}_j^{\widetilde{q}}(v)$, $k = (\widetilde{n} - 1)i + j$. Thus, the basis

functions on the physical domain Ω are given as $\widetilde{R}_k^{\widetilde{p},\widetilde{q}} \circ \mathbf{F}^{-1}$. An integral over Ω can be now transformed to an integral over $]0,1[^2$ as

$$\iint_{\Omega} f(x,y)\,\mathrm{d}x\,\mathrm{d}y = \int_0^1 \int_0^1 f(x(u,v),y(u,v))\,\det(\mathbf{J})\,\mathrm{d}u\,\mathrm{d}v, \qquad (5)$$

where $\mathbf{J}$ is the Jacobian of the variable transformation $\mathbf{F}$, and we have assumed that $\det(\mathbf{J}) > 0$. Note that the knot vectors $\widehat{\boldsymbol{\Xi}}_u$ and $\widehat{\boldsymbol{\Xi}}_v$ used for the parametrization of Ω may be "finer" than the four knot vectors $\boldsymbol{\Xi}_\ell$ $(\ell = 1,\ldots,4)$ used in the parametrization of the domain boundary $\partial\Omega$. The "refinement" is achieved by inserting new knots into the two pairs of knot vectors $(\boldsymbol{\Xi}_1, \boldsymbol{\Xi}_3)$ and $(\boldsymbol{\Xi}_2, \boldsymbol{\Xi}_4)$ respectively. Furthermore, to ensure that we can approximate functions in $H^1(\Omega)$ [20] sufficiently well, we may want to use an even finer (when compared to $\widehat{\boldsymbol{\Xi}}_u$ and $\widehat{\boldsymbol{\Xi}}_v$) pair of knot vectors $\widetilde{\boldsymbol{\Xi}}_u$ and $\widetilde{\boldsymbol{\Xi}}_v$ for the analysis, see Fig. 4. As a consequence of the formula (5), one may evaluate integrals over Ω entering the variational form of a given boundary value problem by computing the integrals over the parameter domain instead. Thus an "IGA assembly routine" may be implemented as a loop over elements defined by the knot vectors $\widetilde{\boldsymbol{\Xi}}_u$ and $\widetilde{\boldsymbol{\Xi}}_v$, see Fig. 4.

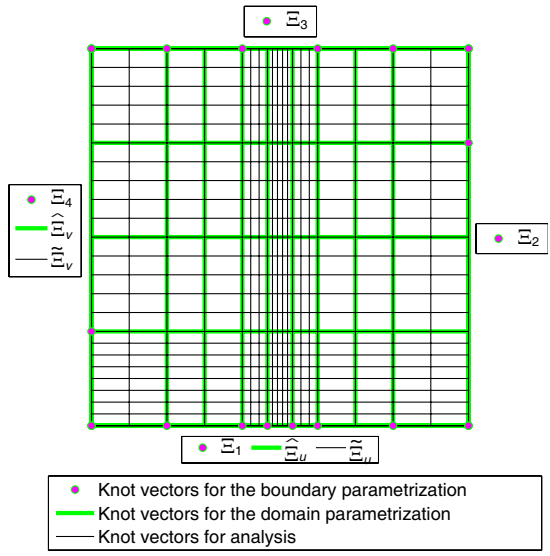

Figure 4. Three types of knot vectors of an IGA model used in the present work.

2.2.3. Galerkin Discretization

An approximation to the solution H_z to (1) is expanded in terms of the basis functions as $H_z = \sum_k h_k \, (\widetilde{R}_k^{\widetilde{p},\widetilde{q}} \circ \mathbf{F}^{-1}) = [\widetilde{R}_1^{\widetilde{p},\widetilde{q}} \circ \mathbf{F}^{-1}, \ldots, \widetilde{R}_{\widetilde{m}\widetilde{n}}^{\widetilde{p},\widetilde{q}} \circ \mathbf{F}^{-1}]\mathbf{h}$, where $\mathbf{h}$ contains all the coordinates of H_z with respect to the selected basis. Substituting this expression into the weak form (2) and utilizing the basis functions as the test functions, we arrive at the following system of linear algebraic equations:

$$(\mathbf{K} + \mathbf{M} + \mathbf{S} + \mathbf{T})\,\mathbf{h} = \mathbf{f}. \tag{6}$$

Entries of the matrices entering (6) are with the help of (5) calculated as follows:

$$\mathbf{K}_{k\ell} = \iint\limits_{]0,1[^2} \frac{1}{\varepsilon_{cr}} \left[\mathbf{J}^{-\mathrm{T}} \nabla \widetilde{R}_k^{\widetilde{p},\widetilde{q}}\right]^{\mathrm{T}} \left[\mathbf{J}^{-\mathrm{T}} \nabla \widetilde{R}_\ell^{\widetilde{p},\widetilde{q}}\right] \det(\mathbf{J})\,\mathrm{d}u\,\mathrm{d}v, \tag{7a}$$

$$\mathbf{M}_{k\ell} = -k_0^2 \iint\limits_{]0,1[^2} \mu_r \, \widetilde{R}_k^{\widetilde{p},\widetilde{q}} \, \widetilde{R}_\ell^{\widetilde{p},\widetilde{q}} \, \det(\mathbf{J})\,\mathrm{d}u\,\mathrm{d}v, \tag{7b}$$

$$\mathbf{S}_{k\ell} = -jk_0 \int\limits_{\mathbf{F}^{-1}(\Gamma_s)} \frac{\mu_r^s}{\varepsilon_{cr}^s} \, \widetilde{R}_k^{\widetilde{p},\widetilde{q}} \, \widetilde{R}_\ell^{\widetilde{p},\widetilde{q}} \,\mathrm{d}s, \tag{7c}$$

$$\mathbf{T}_{k\ell} = \left(jk_0 + \frac{1}{2r_t}\right) \int\limits_{\mathbf{F}^{-1}(\Gamma_t)} \frac{1}{\varepsilon_{cr}} \, \widetilde{R}_k^{\widetilde{p},\widetilde{q}} \, \widetilde{R}_\ell^{\widetilde{p},\widetilde{q}} \,\mathrm{d}s, \tag{7d}$$

$$\mathbf{f}_\ell = \int\limits_{\mathbf{F}^{-1}(\Gamma_t)} \frac{1}{\varepsilon_{cr}} \left(\frac{\partial H_z^i}{\partial \mathbf{n}} + \left(jk_0 + \frac{1}{2r_t}\right) H_z^i\right) \widetilde{R}_\ell^{\widetilde{p},\widetilde{q}} \,\mathrm{d}s, \tag{7e}$$

$$k, \ell = 1, \ldots, \widetilde{m}\widetilde{n}.$$

2.3. B-spline Parametrization

In this section, we recall techniques for handling spline parametrizations in IGA, which will be heavily utilized in Section 3. For more details, see [6, 15].

2.3.1. Validating a B-spline Parametrization

In order to ensure that a given choice of inner control points $\widehat{\mathbf{d}}_{i,j}$, $i = 1, \ldots, \widehat{n}$, $j = 1, \ldots, \widehat{m}$ results in a valid B-spline parametrization of Ω we employ the following approach. The determinant of the Jacobian

of $\mathbf{F}$ given by (4) is computed as

$$\det(\mathbf{J}) = \sum_{i,j=1}^{\widehat{m},\widehat{n}} \sum_{k,\ell=1}^{\widehat{m},\widehat{n}} \det\left[\widehat{\mathbf{d}}_{i,j}, \widehat{\mathbf{d}}_{k,\ell}\right] \frac{\mathrm{d}\widehat{M}_i^p(u)}{\mathrm{d}u} \widehat{N}_j^q(v) \widehat{M}_k^p(u) \frac{\mathrm{d}\widehat{N}_\ell^q(v)}{\mathrm{d}v}, \quad (8)$$

where $\det[\widehat{\mathbf{d}}_{i,j}, \widehat{\mathbf{d}}_{k,\ell}]$ is the determinant of the 2×2 matrix with columns $\widehat{\mathbf{d}}_{i,j}$, $\widehat{\mathbf{d}}_{k,\ell}$. Equation (8) defines a piecewise polynomial of degree $2p-1$ in u and degree $2q-1$ in v, which is C^{p-2} in u and C^{q-2} in v. Such a map can be expanded in terms of B-splines $\mathcal{M}_k^{2p-1}$ and $\mathcal{N}_\ell^{2q-1}$ of degree $2p-1$ and $2q-1$ with the knot vectors obtained from $\widehat{\boldsymbol{\Xi}}_u$ and $\widehat{\boldsymbol{\Xi}}_v$ by raising the multiplicities of the inner u-knots and v-knots by p and q, respectively [24]. That is,

$$\det(\mathbf{J}) = \sum_{k,\ell=1}^{M,N} c_{k,\ell}\, \mathcal{M}_k^{2p-1}(u)\, \mathcal{N}_\ell^{2q-1}(v), \quad (9)$$

where the coefficients $c_{k,\ell}$ depend linearly on the quantities $\det[\widehat{\mathbf{d}}_{i,j}, \widehat{\mathbf{d}}_{k,\ell}]$. As B-splines are non-negative, we conclude that whenever all the coefficients $c_{k,\ell}$ are positive (or negative), so is the quantity $\det(\mathbf{J})$.

2.3.2. Constructing a Reference B-spline Parametrization

None of the linear methods (such as for example those presented in [6]) for extending the parametrization of the boundary into the interior of the domain can in general guarantee that the resulting map $\mathbf{F}$ will satisfy $\det(\mathbf{J}) > 0$ everywhere on $]0,1[^2$. Therefore, during some shape optimization iterations we have to utilize a more expensive non-linear method for improving the distribution of the interior control points $\widehat{\mathbf{d}}_{i,j}$. In a view of (9), we can obtain a parametrization by solving the following optimization problem:

$$\begin{aligned} &\underset{\text{inner } \widehat{\mathbf{d}}_{i,j}, z}{\text{maximize}} && z, \\ &\text{subject to} && c_{k,\ell}\big(\widehat{\mathbf{d}}_{i,j}\big) \geq z, \end{aligned} \quad (10)$$

where $\widehat{\mathbf{d}}_{i,j}$ are inner control points as stated in (4). $c_{k,\ell}$ are given by (9), and z is an auxiliary optimization variable. If z resulting from approximately solving (10) to local optimality is positive then we are guaranteed to have a valid parametrization. Unfortunately, the quality of the parametrization obtained in this fashion needs not to be very high. So we improve the parametrization by making it as conformal as

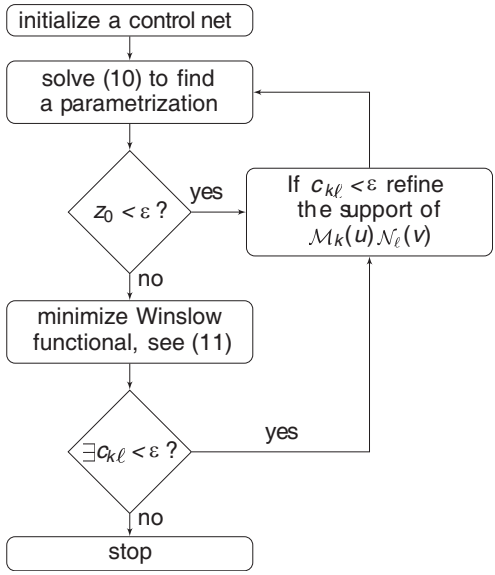

Figure 5. The algorithm for extending a boundary parametrization to the interior. ε is a small parameter of the algorithm. In this work, we use $\varepsilon = 10^{-5}$.

possible. This is done by solving the following constrained optimization problem:

$$\begin{aligned} &\underset{\text{inner } \widehat{\mathbf{d}}_{i,j}}{\text{minimize}} \quad \int_0^1 \int_0^1 W\left(\widehat{\mathbf{d}}_{i,j}\right) \mathrm{d}u\, \mathrm{d}v, \\ &\text{subject to} \quad c_{k\ell}\left(\widehat{\mathbf{d}}_{i,j}\right) \geq 0, \end{aligned} \tag{11}$$

where $W(\widehat{\mathbf{d}}_{i,j}) = (\|\mathbf{F}_u\|^2 + \|\mathbf{F}_v\|^2)/\det[\mathbf{F}_u, \mathbf{F}_v]$ is referred to as the Winslow functional [14].

In our numerical experiments we utilize the interior point algorithm constituting a part of Optimization Framework in Matlab [25] for solving the optimization problems (10) and (11) to approximate stationarity. The whole process is outlined in Fig. 5.

2.3.3. Quadratic Approximation of the Winslow Functional

For the purpose of reparametrizing the domain from one shape optimization iteration to another the algorithm based on finding minima of Winslow functional is unnecessarily computationally burdensome. To remedy this we chose to minimize a second order

Taylor series approximation of Winslow functional:

$$\mathcal{W}\left(\widehat{\mathbf{d}}\right) = \iint_{\Omega} W\left(\widehat{\mathbf{d}}\right) \mathrm{d}u\mathrm{d}v \approx \mathcal{W}\left(\widehat{\mathbf{d}}_0\right) + \left(\widehat{\mathbf{d}} - \widehat{\mathbf{d}}_0\right)^{\mathrm{T}} \mathbf{G}\left(\widehat{\mathbf{d}}_0\right) + \frac{1}{2}\left(\widehat{\mathbf{d}} - \widehat{\mathbf{d}}_0\right)^{\mathrm{T}} \mathbf{H}\left(\widehat{\mathbf{d}}_0\right)\left(\widehat{\mathbf{d}} - \widehat{\mathbf{d}}_0\right), \quad (12)$$

where $\widehat{\mathbf{d}}$ is a vector with all control points $\widehat{\mathbf{d}}_{i,j}$ and $\widehat{\mathbf{d}}_0$ the control points for a reference parametrization obtained by solving (11). $\mathbf{G}$ and $\mathbf{H}$ are the gradient and Hessian of $\mathcal{W}$.

The necessary optimality conditions for minimizing the right hand side of (12) define an affine mapping between the boundary and the interior control points thereby providing us with a fast method for computing the domain parametrization and its derivatives with respect to the boundary control points.

2.3.4. Multiple Patches

In many practical situations the computational domain is not parametrized by a single patch only. Similarly to the single-patch case, the parametrization of the domain boundary is given, and the task of extending the parametrization into the interior remains the same with the exception that the parametrization of inter-patch boundaries is unknown. Control points corresponding to these boundaries become additional variables in the optimization problems (10), (11), and the quadratic approximation of the latter, whereas C^0-continuity requirement for the parametrization across the inter-patch boundaries introduces auxiliary linear equality constraints. The overall algorithmic structure remains unchanged.

3. OPTIMIZATION OF THE SHAPE OF THE SCATTERER

3.1. Statement of the Shape Optimization Problem

We consider the problem of finding shapes of metallic scatterers depicted in Fig. 2 in order to maximize the following quantity, which is proportional to the time-averaged magnetic energy:

$$W_{\square} = 2 \int_{\Omega_{\square}} |H_z|^2 \, \mathrm{d}V, \quad (13)$$

where H_z is the solution to Equation (1). The domain $\Omega_{\square}$ in (13) is a small rectangular region between the two scatterers, see Fig. 2. In (13), the factor 2 accounts for the fact that we only integrate over a

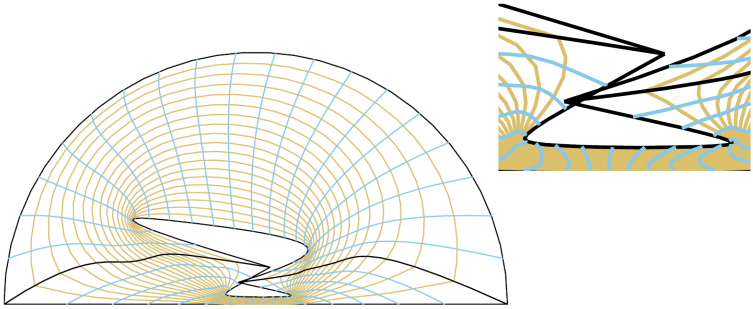

Figure 6. When no additional regularity conditions are imposed, the scatterer's boundary tends to approach the truncation boundary and to self-intersect.

half of the symmetric domain. The only difference between the problem studied in Aage et al. [16] and the one studied in this paper is that we maximize magnetic energy in a small rectangular region and not in a small circular region. However, in order to compare the efficiency of our design with the one found in Aage et al. [16] we later evaluate the magnetic energy in the circular region as well.

In order to avoid non-physical situations and to prevent numerical complications, see Fig. 6, we introduce three constraints on the family of considered shapes. Namely, we impose a minimum vertical distance between the two scatterers, forbid self-intersections of the boundary, and also enforce an upper limit on its volume.

3.2. Isogeometric Shape Optimization Algorithm

In this section, we formulate the optimization problem stated in Section 3.1 in an isogeometric analysis context. We then derive differentiable constraints to prevent the shape of the scatterer from self-intersecting. Finally, we present the expressions for derivatives (sensitivities) of the shape-dependent functions involved in the problem with respect to boundary control points.

We parametrize the physical domain by the 2-patch model shown in Fig. 10. The overall optimization strategy that we utilize is outlined in Fig. 7.

3.3. Objective Function

Let $\mathbf{F}$ be the parametrization of the physical domain given by (4). The energy $W_\square$ given by (13) now becomes

$$W_\square = 2\int_{\Omega_\square} |H_z|^2 \,\mathrm{d}V = 2\iint_{\mathbf{F}^{-1}(\Omega_\square)} |H_z \circ \mathbf{F}|^2 \,\det(\mathbf{J})\,\mathrm{d}u\,\mathrm{d}v$$
$$= 2\iint_{\mathbf{F}^{-1}(\Omega_\square)} \left|\left[\widetilde{R}_1^{\widetilde{p},\widetilde{q}},\ldots,\widetilde{R}_{\widetilde{m}\widetilde{n}}^{\widetilde{p},\widetilde{q}}\right]\mathbf{h}\right|^2 \det(\mathbf{J})\,\mathrm{d}u\,\mathrm{d}v\,. \tag{14}$$

To simplify the computation of the quantity $W_\square$, we chose the region $\Omega_\square$ as one knot span, see Fig. 10. We keep the parametrization of this region fixed throughout all optimization iterations, that is, the region is independent from the design variables, and we choose the region's control points so that $\Omega_\square$ is a rectangle, see Figs. 2, 9 and 10. As $W_\square$ changes by several orders of magnitude throughout the course of the computations we minimize $\log_{10}(W_\square)$ instead.

3.4. Constraints

To enforce a lower bound on the vertical placement of the scatterer we impose a lower bound on the ordinates of the design control

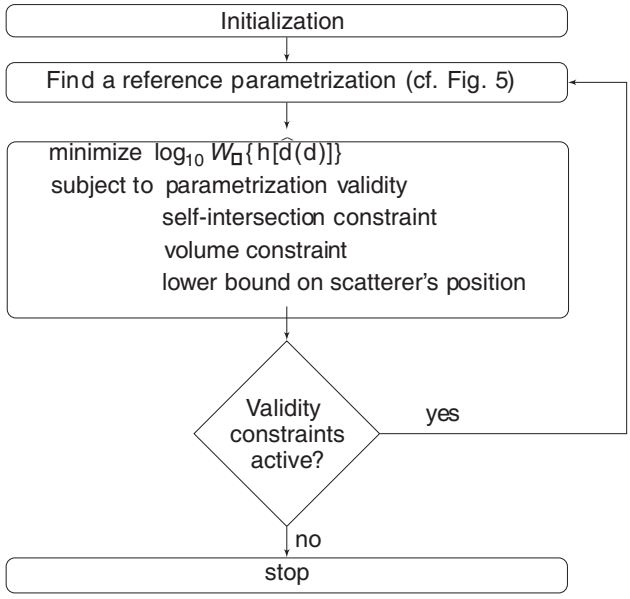

Figure 7. The isogeometric shape optimization algorithm used in the current work.

points, see Fig. 9. The lower bound used in the present paper is 0.1 [m]. Additionally, we include the non-negativity requirement for the Jacobian expansion coefficients $c_{k,\ell}(\widehat{\mathbf{d}})$, see (9) as constraints. We now investigate the remaining constraints mentioned in Section 3.1.

3.4.1. Self-intersection Constraint

Let $N_i(\xi)$ $(i = 1, \ldots, n)$ be B-splines of degree p with a knot vector $\boldsymbol{\Xi}$. Consider a B-spline curve $\mathbf{r}(\xi) = \sum_i \mathbf{d}_i N_i(\xi)$, where $\mathbf{d}_i$ are design control points. To ensure that $\mathbf{r}$ does not intersect itself, we look at the square distance between every pair of points on the curve, $(\mathbf{r}(u), \mathbf{r}(v))$, $(u, v) \in \boldsymbol{\Xi} \times \boldsymbol{\Xi}$. That is

$$\begin{aligned} d^2_{\mathbf{r}}(u, v) &= \|\mathbf{r}(u) - \mathbf{r}(v)\|^2 \\ &= \sum_{i,j} \mathbf{d}_i \cdot \mathbf{d}_j \big(N_i(u) - N_i(v)\big)\big(N_j(u) - N_j(v)\big). \end{aligned} \tag{15}$$

Clearly, the curve is simple if and only if $d^2_{\mathbf{r}}(u, v) > 0$ for every $u \neq v$, $u, v \in [0, 1]^2$. To ensure that this condition is fulfilled, we look at rectangles in $[0, 1]^2$ formed by the products of knot spans, see Fig. 8. First, consider a rectangle $\Omega_a = [\xi_k, \xi_{k+1}] \times [\xi_\ell, \xi_{\ell+1}]$ that does not intersect the diagonal $\{(u, v) : u = v\}$. In Ω_a, $d^2_{\mathbf{r}}(u, v)$ can be expressed in terms of the Bernstein polynomials [23] of degree $2p$,

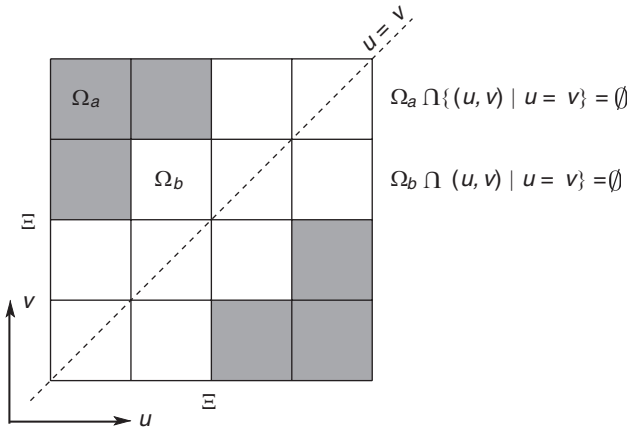

Figure 8. A knot vector Ξ partitions the unit square $[0, 1]^2$ into products of knot spans. We classify the rectangles according to whether they intersect the diagonal or not.

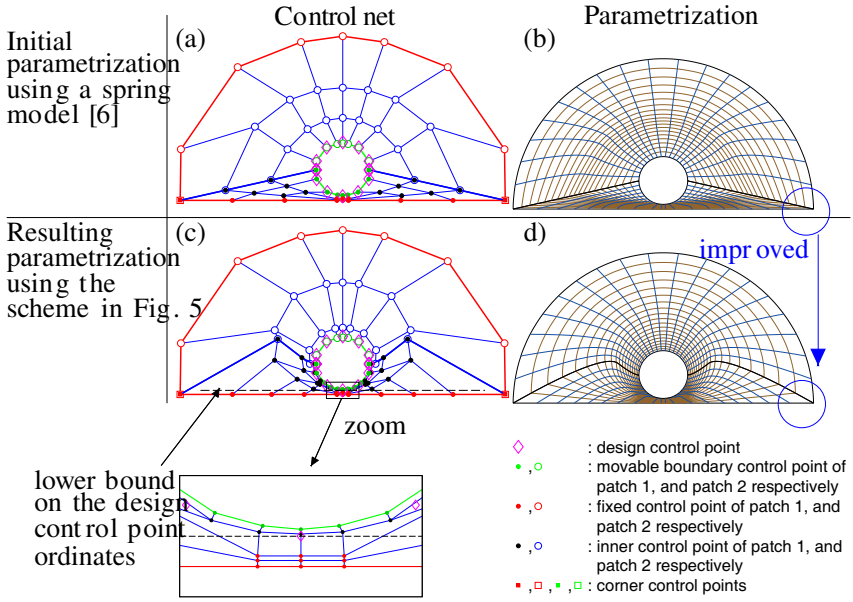

Figure 9. Initial shape used for the optimization, and a comparison between two parametrizations of this domain. Interestingly enough, the excessively acute angle in one corner of patch 1 shown in (b) is improved in (d). The agreements of parameter lines in (b) and (d) illustrate the C^0-continuity of the parametrization, despite possible disagreements of knot vectors. Below (c), a zoom near the energy harvesting region shows a set of fixed control points (in red). The parametrization is frozen in this area thereby simplifying the task of evaluating the objective function and its sensitivity.

$B_\alpha^{2p}(t) = \binom{2p}{\alpha}(1-t)^{2p-\alpha}t^\alpha$, $\alpha = 0, \ldots, 2p$. To be precise

$$d_{\mathbf{r}}^2(u,v) = \sum_{\alpha,\beta=0}^{2p} a_{\alpha,\beta} B_\alpha^{2p}\left(\frac{u-\xi_k}{\xi_{k-1}-\xi_k}\right) B_\beta^{2p}\left(\frac{v-\xi_\ell}{\xi_{\ell-1}-\xi_\ell}\right). \tag{16}$$

Note that the basis functions B_α^{2p} are non-negative and that the value of $d_{\mathbf{r}}^2$ at the corners (ξ_i, ξ_j), $i = k,\ k+1$, and $j = \ell,\ \ell+1$, are equal to the corner control points $a_{0,0}$, $a_{0,2p}$, $a_{2p,0}$, and $a_{2p,2p}$. Therefore, the squared distance will be positive provided that the following conditions are satisfied

$$a_{\alpha,\beta} \geq 0\,, \qquad \alpha,\beta = 0,\ldots,2p\,, \tag{17}$$

$$a_{\alpha,\beta} \geq \delta\,, \qquad \alpha,\beta = 0,2p\,, \tag{18}$$

where δ is a small positive number. Four of the conditions in (17) are of course implied by (18) and can be omitted.

For a rectangle $\Omega_b = [\xi_k, \xi_{k+1}] \times [\xi_\ell, \xi_{\ell+1}]$ intersecting the diagonal, the only difference from the previously described situation is that $(u-v)^2$ is a factor of $d_{\mathbf{r}}^2$. Therefore, the expansion (16) can now be replaced by

$$\frac{d_{\mathbf{r}}^2(u,v)}{(u-v)^2} = \sum_{\alpha,\beta=0}^{2p-2} b_{\alpha,\beta} B_\alpha^{2p-2}\left(\frac{u-\xi_k}{\xi_{k-1}-\xi_k}\right) B_\beta^{2p-2}\left(\frac{v-\xi_\ell}{\xi_{\ell-1}-\xi_\ell}\right). \quad (19)$$

If we replace $a_{\alpha,\beta}$ with $b_{\alpha,\beta}$ and p with $p-1$ in (17) and (18) we obtain sufficient conditions in this case too.

Note that utilizing the invariance of (15) with respect to changing the roles of u and v, only one half of the conditions is needed. Also, similarly to (A2), the coefficients $a_{\alpha,\beta}$ in (16) and $b_{\alpha,\beta}$ in (19) may be explicitly represented as quadratic forms of the design control points $\mathbf{d}_i$. We emphasize that these conditions are sufficient but not necessary for the boundary to be a simple curve. At the same time, knot insertions can be used to obtain tighter conditions.

For the current optimization problem, the scatterer's boundary is composed of two B-spline curves, but the conditions above are extended to such a case in a straightforward manner.

3.4.2. Volume Constraint

Utilizing the divergence theorem, the restriction on the volume of the scatterer may be written as a boundary integral

$$\frac{1}{2}\oint_{\partial D} \det[\mathbf{r}, \dot{\mathbf{r}}]\, \mathrm{d}\Gamma \le V_0\,. \quad (20)$$

In (20), D is the domain inside the scatterer, $\mathbf{r}$ a parametrization of the boundary ∂D of D, V_0 a volume limit, and $\det[\mathbf{r}, \dot{\mathbf{r}}]$ the determinant of the matrix with columns $\mathbf{r}$ and $\dot{\mathbf{r}}$. The positive orientation of the line integral in (20) is counterclockwise. In this paper, we choose the same volume limit as that in [16]: $V_0 = \pi 0.65^2$ [m^2]. If $\mathbf{r}(\xi) = \sum_i \mathbf{d}_i N_i(\xi)$, the integral in (20) is computed as

$$\oint_{\mathbf{r}([0,1])} \det[\mathbf{r}, \dot{\mathbf{r}}]\, \mathrm{d}\Gamma = \sum_{i,j} \det[\mathbf{d}_i, \mathbf{d}_j] \int_0^1 N_i(\xi)\, \dot{N}_j(\xi)\, \mathrm{d}\xi\,. \quad (21)$$

3.5. Sensitivity Analysis

In order to utilize standard mathematical programming techniques for solving the optimization subproblem (cf. Fig. 7) we need to

compute the derivatives (sensitivities) of the objective function and the constraints with respect to our design variables, that is, components of the vector of the boundary control points $\mathbf{d}$. This amounts to applying the chain rule and the inverse function theorem to the problem (6).

Both the self-intersection constraints (cf. Subsection 3.4.1) and the volume constraint (cf. Subsection 3.4.2) are quadratic functions of design variables $\mathbf{d}$, rendering the calculation of their partial derivatives to be a straightforward task.

The domain parametrization validity constraints (cf. Subsection 2.3.1), on the other hand, are quadratic functions of the inner control points $\widehat{\mathbf{d}}$. Therefore we also need to compute the partial derivatives $\partial\widehat{\mathbf{d}}/\partial\mathbf{d}$. However, owing to the affine dependence of the interior control points $\widehat{\mathbf{d}}$ on the boundary control points $\mathbf{d}$ through the stationarity conditions for minimizing the quadratic form (12) this computation amounts to Gaussian elimination.

It only remains to differentiate the objective function (14). Recalling that $\mathbf{F}^{-1}(\Omega_\square)$ and consequently $\mathbf{J}\big|_{\mathbf{F}^{-1}(\Omega_\square)}$ is independent from $\widehat{\mathbf{d}}$, we can write

$$\frac{\partial W_\square}{\partial \widehat{d}_i} = 4 \iint_{\mathbf{F}^{-1}(\Omega_\square)} \operatorname{Re}\left\{ \frac{\partial (H_z \circ \mathbf{F})}{\partial \widehat{d}_i}\, \overline{H_z \circ \mathbf{F}} \right\} \det(\mathbf{J})\, \mathrm{d}u\, \mathrm{d}v\,. \tag{22}$$

In turn, we compute the partial derivative $\partial(H_z \circ \mathbf{F})/\partial\widehat{d}_i$ as

$$\frac{\partial (H_z \circ \mathbf{F})}{\partial \widehat{d}_i} = \left[\widetilde{R}_1^{\widetilde{p},\widetilde{q}}, \ldots, \widetilde{R}_{\widetilde{m}\widetilde{n}}^{\widetilde{p},\widetilde{q}} \right] \frac{\partial \mathbf{h}}{\partial \widehat{d}_i}\,. \tag{23}$$

The quantity $\frac{\partial \mathbf{h}}{\partial \widehat{d}_i}$ is obtained by differentiating the discretized Helmholtz Equation (6):

$$(\mathbf{K} + \mathbf{M} + \mathbf{S} + \mathbf{T}) \frac{\partial \mathbf{h}}{\partial \widehat{d}_i} = -\frac{\partial (\mathbf{K} + \mathbf{M} + \mathbf{S})}{\partial \widehat{d}_i} \mathbf{h}\,, \tag{24}$$

where we utilized the fact that $\frac{\partial \mathbf{T}}{\partial \widehat{d}_i} = \frac{\partial \mathbf{f}}{\partial \widehat{d}_i} = \mathbf{0}$. Finally, the partial derivatives of $\mathbf{K}$, $\mathbf{M}$, and $\mathbf{S}$ are calculated by differentiating (7).

4. NUMERICAL EXAMPLES

We begin this section by specifying physical and optimization parameters used in the present numerical experiments. We then present the results of shape optimization of conducting scatterers with the IGA-based shape optimization algorithm described earlier. Different fineness levels of analysis (meshing) for computing a model response numerically in each optimization iteration are carefully chosen for different stages of the optimization problem.

Table 1. Electromagnetic constants used in this work.

electromagnetic constants of air	electromagnetic constants of copper
$\varepsilon_r = 1$	$\varepsilon_r^s = 1$
$\mu_r = 1$	$\mu_r^s = 1$
—	$\sigma = 10^6$ [S/m]

4.1. Technical Remarks and Optimization Parameters

We list here a few technical remarks. For the sake of computational efficiency, the matrices of the quadratic forms in (9), (21), (16), and (19) as well as the fixed matrices $\mathbf{T}$, $\mathbf{f}$ in (6) are pre-computed and stored before the optimization process starts. We use standard Gaussian quadratures [26] of order 7 for numerical integration. All the solutions presented in this section have been obtained with gradient based non-linear programming solver *fmincon* from Optimization Framework of Matlab, version 7.9 (R2009b) [25].

In Table 1, we list the physical parameters needed by the present numerical experiments. In the former table, we take all parameters, including the conductivity of copper, from Aage et al. [16] in order to be able to compare the optimal designs.

4.2. Initial Shape and Its Parametrization

We start the optimization using the following sets of knot vectors in the notation of Fig. 4:

$$\begin{aligned}
\boldsymbol{\Xi}_1 &= \left\{0,0,0,\tfrac{1}{5},\tfrac{3}{10},\tfrac{2}{5},\tfrac{7}{15},\tfrac{8}{15},\tfrac{3}{5},\tfrac{7}{10},\tfrac{4}{5},1,1,1\right\},\\
\boldsymbol{\Xi}_3 &= \left\{0,0,0,\tfrac{1}{5},\tfrac{2}{5},\tfrac{3}{5},\tfrac{4}{5},1,1,1\right\},\\
\boldsymbol{\Xi}_2 &= \boldsymbol{\Xi}_4 = \left\{0,0,0,\tfrac{1}{2},1,1,1\right\},\\
\widehat{\boldsymbol{\Xi}}_u &= \boldsymbol{\Xi}_1,\ \widehat{\boldsymbol{\Xi}}_v = \boldsymbol{\Xi}_2,
\end{aligned}$$

for parametrizing the two patches. Unless explicitly stated otherwise, all B-splines used in the present experiment are quadratic. For the initial shape, we use a piecewise spline approximation, see Appendix A, of the circle with center at $(0, 0.75)$ and radius $r = 0.65\,[\mathrm{m}]$, as in [16] by Aage et al. For the truncation boundary, we utilize the spline approximation of the upper half of the circle with center at $(0, 0)$ and radius $r_t = 4\,[\mathrm{m}]$ depicted in Fig. A1. Note that the electrical condition [27] at the truncation boundary is fulfilled because

$kr_t = 9.6438 \gg 1$, where k is the wavenumber of the incoming wave in air.

Having the parametrization of the initial scatterer shape and the truncation boundary, we extend it to a parametrization of the entire domain using a spring model [6]. Feeding the resulting parametrization, see Figs. 9(a), (b), to the parametrization routine in Fig. 5, we obtain the parametrization shown in Figs. 9(c), (d). Importantly, new knots have been inserted to the domain parametrization knot vectors of patch 2. The new knots could be seen as the differences between the two sets of knot vectors in Fig. 10. Note that for a multiple patch model, the refinement constraints along common boundary components are required in order to have a *continuous* parametrization of the entire domain.

If we during the optimization need to refine the knot vectors for the parametrization we may also need to refine the knot vectors for the analysis, see Fig. 5. The insertion rule we apply is illustrated in Fig. 10. Moreover, in order to accurately approximate the numerical solution in the energy harvesting region $\Omega_\square$ we would like to refine the parametrization locally around this region. Fortunately the special "horizontally dominant" geometry of the patch 1 allows us to easily fulfill this requirement. Indeed, the local refinement is carried out by inserting many knots in the area whose image is near $\Omega_\square$, and using a finer analysis knot vector for the patch 1 than for the patch 2, see Fig. 10.

4.3. Shape Optimization Results

We now feed the initial setting discussed in Section 4.2 to the optimization routine outlined in Fig. 7. The optimization algorithm terminates successfully after 141 iterations. Throughout this process, there are nine times when *fmincon* is terminated and we need to update the reference parametrization and analysis. In the notation of Fig. 10 the analysis mesh for the last step of the diagram in Fig. 7 is given by $(k_1, k_2, k_3, k_4, k_5) = (99, 59, 13, 13, 13)$, $(\ell_1, \ell_2, \ell_3) = (3, 15, 9)$ for patch 1, and $k = 19$, $(\ell_1, \ell_2, \ell_3) = (3, 15, 9)$ for patch 2. The number of DOFs in the corresponding analysis is 16948. In Fig. 11, we show the scatterers where the parametrization needs to be updated, as well as the final optimized one.

In order to compare the performance in terms of energy concentration between the resulting scatterer and the initial scatterer, we use COMSOL Multiphysics [28] to solve the governing Equation (1) with FEM. The comparison is depicted in Fig. 12. According to this, the resulting scatterer clearly outperforms the initial one. Indeed, the magnetic energy with the presence of the resulting scatterer is highly

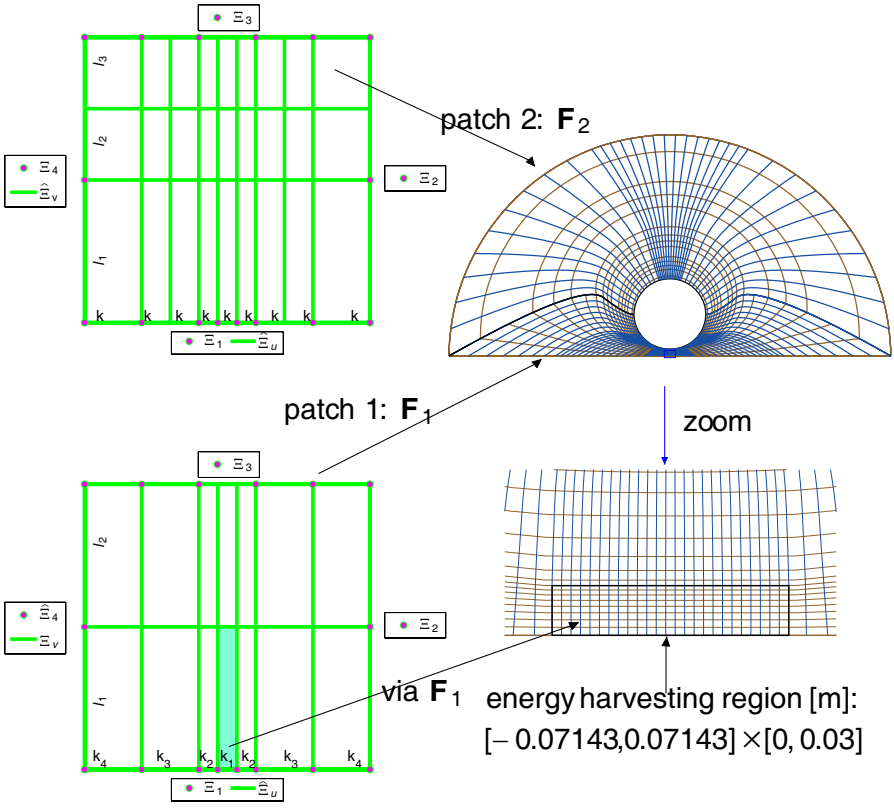

Figure 10. The initial analysis model of the optimization. Two different sets of knot vectors are employed to parametrize the two patches comprising of the physical domain. The knot vector notations are given by Fig. 4. The numbers $k_1, \ldots, k_4$, k and ℓ_1, ℓ_2 indicate the numbers of additional knots uniformly inserted into the corresponding knot spans to generate analysis knot vectors. For the initial (or a general) model, we use $(k_1, \ldots, k_4[, k_5, \ldots]) = (24, 14, 6, 6[, 6, \ldots])$, $(\ell_1, \ell_2[, \ell_3, \ldots]) = (0, 7[, 4, \ldots])$ for patch 1, and $k = 4$, $(\ell_1, \ell_2, \ell_3[, \ell_4 \ldots]) = (0, 5, 3[, 3, \ldots])$ for the other. The analysis configuration results in a model with 2612 degrees of freedom.

concentrated in the energy harvesting region with a maximum intensity at a factor of 10^4 times stronger than that of the circular scatterer.

To provide some physical insight into the performance of the resulting scatterer, we solve the eigenvalue problem corresponding to (1a) with homogeneous Dirichlet boundary condition on the truncation boundary Γ_t and the homogeneous Neumann boundary

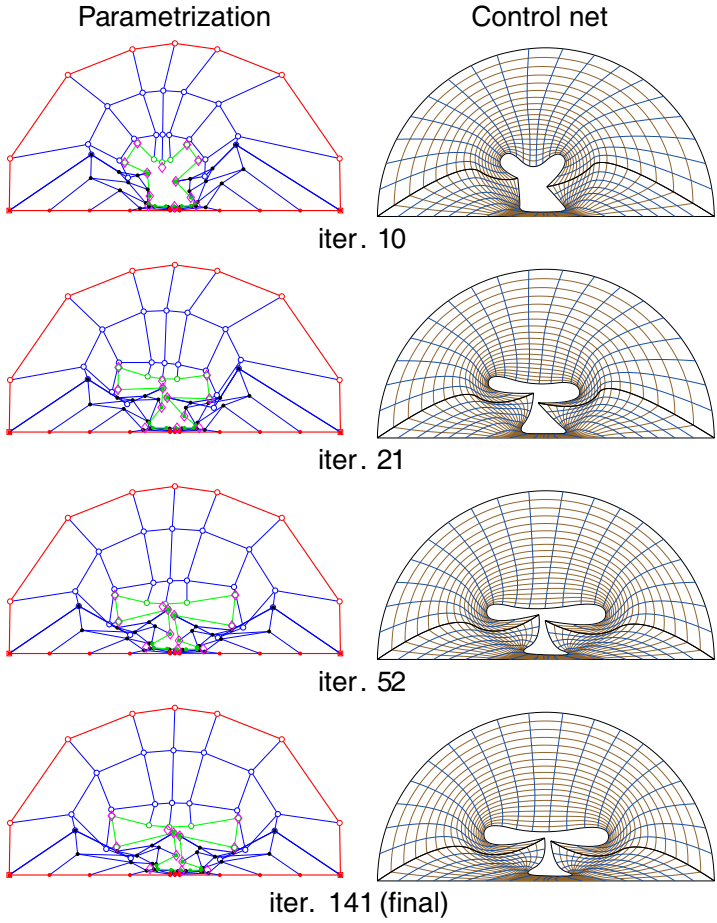

Figure 11. Snapshots of the control nets and parametrizations at some iterations where the outer optimization algorithm is stopped in order to update the reference parametrization (see Fig. 5).

condition on the scatterer's interface Γ_s, see Fig. 2. The later boundary condition corresponds to assuming that the scatterer is a perfect electric conductor. Interestingly enough, one of the modes, u_{13}, looks strikingly similar to the solution $u = H_z$ shown in Fig. 13(a), and the corresponding eigenfrequency $f_{13} = 1.14987 \times 10^8$ [Hz] differs only by 0.01% from the frequency of the incident wave $f = 1.15 \times 10^8$ [Hz]. By calculating the L^2-projection of the solution u on the eigenfunctions u_i

$$c_i = \langle u, u_i \rangle = \int_\Omega u\, u_i \, \mathrm{d}V, \tag{25}$$

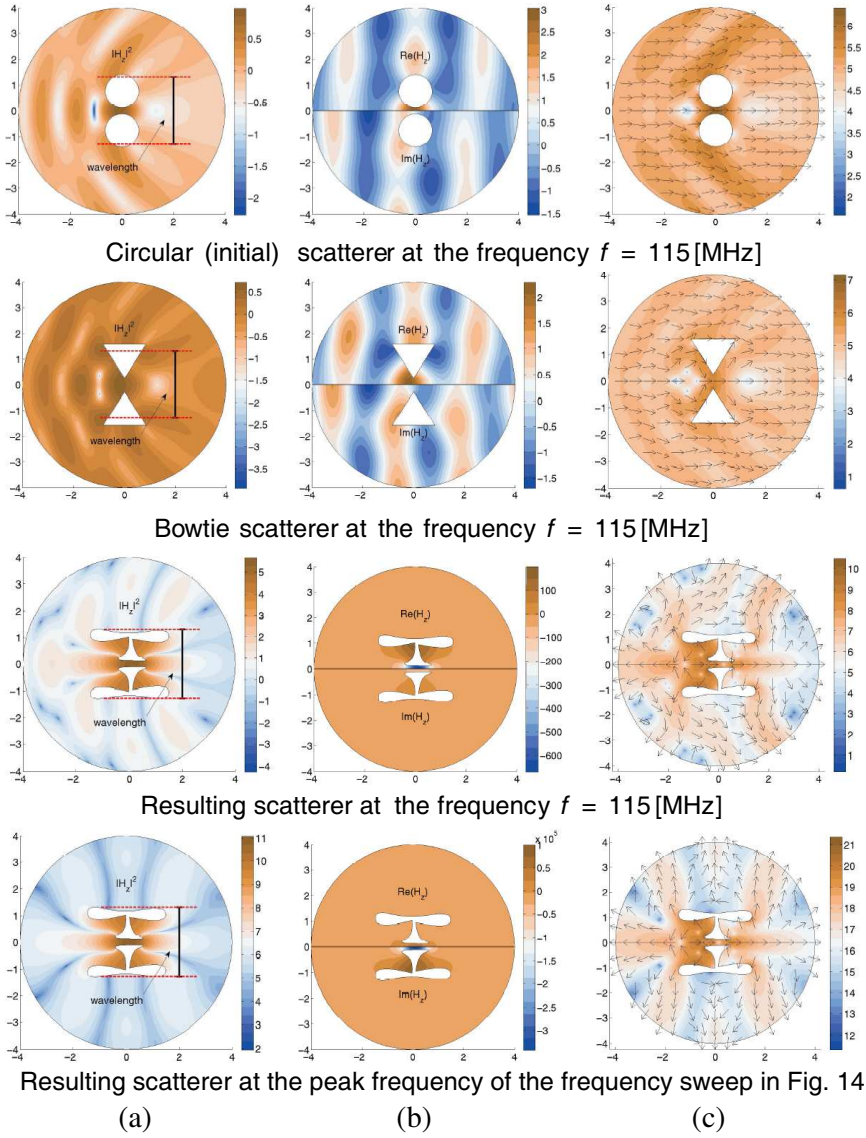

Figure 12. (a) Base-10 logarithm of the normalized time-averaged energy of the magnetic field intensity around the optimized scatterer, i.e., $\log_{10}(|H_z|^2)$. (b) The real and imaginary parts of the field, and (c) time averaged Poynting vectors (color: logarithm of the magnitude, arrows: normalized direction).

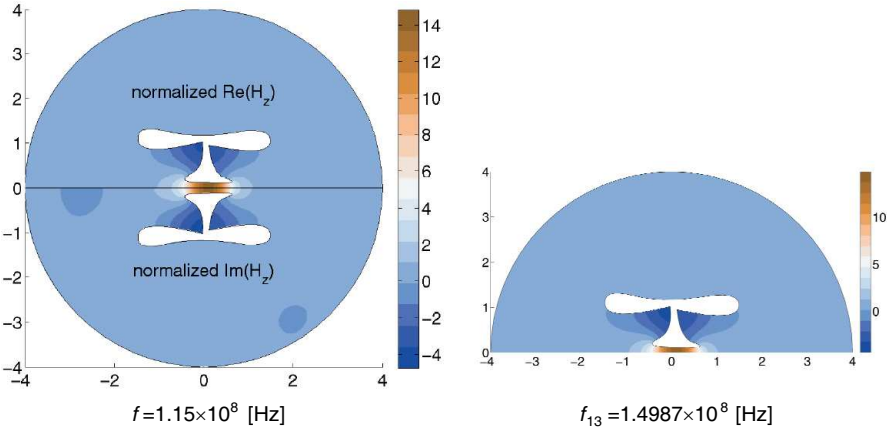

Figure 13. (a) The normalized real and imaginary parts of H_z resulting from the optimized scatterer shape; f is the frequency of the incoming wave. (b) The thirteenth (real) eigenmode of the eigenproblem described in Section 4; f_{13} is the corresponding eigenfrequency.

we find that 98% of the L^2-energy of the solution is contained in the mode u_{13}, that is $|c_{13}|^2/\|u\|^2_{L^2} \approx 0.98$. Thus, the high energy concentration is probably due to a resonance-type phenomenon.

4.4. Comparison with Earlier Designs

To perform a careful comparison of the performance of the scatterer with earlier designs, we perform a frequency sweep in the neighbourhood of the driving frequency $f = 115$ [MHz] while noting the integral of the normalized time-averaged magnetic energy over $\Omega_\circ$: $x^2 + y^2 \leq 0.08^2$ [m]. The same performance measure has been considered in [16]. The results of such a comparison are illustrated in Fig. 14. Since we carried out the optimization only at one frequency with the goal of emphasizing the field in a small spatial region, we may expect a very high Q-factor [29, chapter 9]. This is indeed the case: the scatterer has a Q-factor $Q \approx 8.617 \times 10^6$.

When comparing our results with those found in [16] using topology optimization, we note that in [16] the two scatterers were constrained to be within two circular domains, while in the present situation we allow the scatterers to vary more freely. Furthermore, it should be noted that the frequency sweep reveals that the peak

operational frequency for the scatterer that we computed is slightly shifted from the prescribed driving frequency. This is a well-known issue, e.g., see [16]. Owing to the approximately invariant properties of the problem (1) under simultaneous scaling of the frequency and size, we can easily scale the geometry to obtain the peak at the driving frequency, as has also been done in [16].

Our scaled scatterer concentrates 10^9 times more energy in the harvesting region compared to the one computed in [16]. We note that recently Aage [30] has computed an updated version of the topology optimized scatterer using the bounding box of Fig. 12 as a design domain. This resulted in an improved design with the performance of $\log_{10}(W_{\square}) = 1.4$.

Finally, we compare our design with some well-known magnetic energy resonators including circle-typed scatterers and Bowtie scatterers, see Fig. 12, and Table 2. It is clear that our design also outperforms the well-know configurations by a factor of a billion in terms of magnetic energy concentration in the domain $\Omega_{\circ}$.

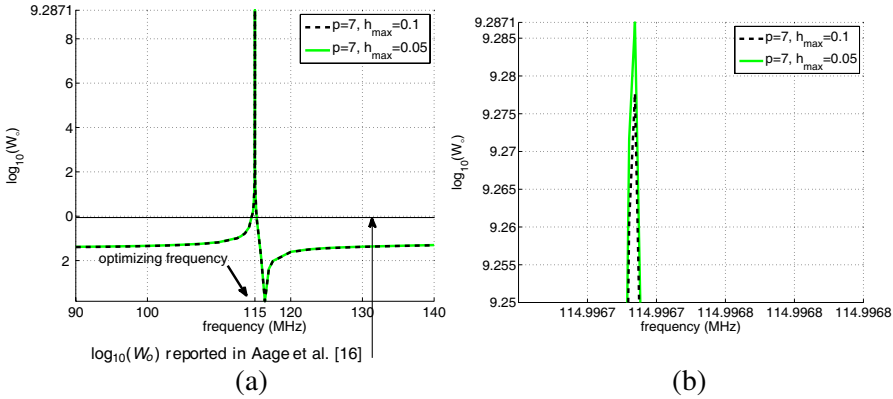

Figure 14. (a) The frequency sweep of the final optimization result and (b) a zoom near the driving frequency. The energy is calculated in the circular domain $\Omega_{\circ}$ to compare results with those from Aage et al. [16]. For the validation purpuses, the graphs are obtained COMSOL Multiphysics [28], on two unstructured meshes (one is approximately double so fine as the other) using Lagrange triangles of the 7th order.

Table 2. Quantitative performance of various scatter configurations.

Design	Circle	Bowtie	Aage et al. [16]	Our design
$\log_{10}(W_\circ)$	-0.9898	-1.0502	-0.07	9.2871

5. CONCLUSIONS

We have computed a novel scatterer shape resulting in a remarkable local magnetic field enhancement using shape optimization and isogeometric analysis. The resulting scatterer shape has increased the energy concentration by a factor of one billion compared to the topology optimization result of Aage et al. [16]. It also has a very high quality factor and thus is very promising for realistic industrial applications despite the two-dimensional idealization.

In addition, we have devised an inexpensive method for extending a B-spline parametrization of the boundary onto the whole computational domain based on minimizing a second order approximation to a Winslow functional. Such a method is an important part of a shape optimization algorithm based on isogeometric analysis. As shown in the paper, the resulting algorithm works well for the benchmark shape optimization problem.

Finally, we have implemented a routine that executes our optimization strategy in an automated way. This is promising and important for the future development of our research code into engineering software.

ACKNOWLEDGMENT

The authors would like to thank Allan Roulund Gersborg, Niels Aage, and Olav Breinbjerg for their valuable input and feedback, which helped us to improve the presentation of the material. DMN would like to gratefully acknowledge the financial support from the European Community's Seventh Framework Programme FP7/2007-2013 under grant agreement n° PITN-GA-2008-214584 (SAGA).

APPENDIX A. B-SPLINE APPROXIMATION OF A CIRCULAR ARC

In this section, we describe the method used in the present work for approximating circular arcs using B-splines. We employ this method for approximating the truncation boundary and the initial shape of the scatterer.

Let $N_i(\xi)$, $i = 1, \ldots, n$, be B-splines of degree p with a knot vector $\boldsymbol{\Xi}$. Consider a B-spline curve $\mathbf{r}(\xi) = \sum_i \mathbf{d}_i N_i(\xi)$ with unknown control points $\mathbf{d}_i$, with which we would like to approximate a given circular arc. Assuming that arc's center is at the origin, we want to maintain the equality $\mathbf{r} \cdot \dot{\mathbf{r}} = 0$, where $\dot{\mathbf{r}}$ denotes the derivative of $\mathbf{r}$ with respect to ξ. Similarly to (9) we write

$$\mathbf{r} \cdot \dot{\mathbf{r}} = \sum_{i,j} \mathbf{d}_i \cdot \mathbf{d}_j N_i \dot{N}_j = \sum_{\alpha} c_\alpha \widetilde{N}_\alpha, \tag{A1}$$

where $\widetilde{N}_\alpha$, $\alpha = 1, \ldots, \widetilde{n}$, are B-splines of degree $2p-1$ with multiplicities of inner knots raised by p. If all $c_\alpha = 0$ in (A1), then so is the quantity $\mathbf{r} \cdot \dot{\mathbf{r}}$.

We now derive explicit expressions for c_α in terms of the vector of the boundary control points $\mathbf{d}$. To this end, let $\{\widetilde{N}^*_\alpha\}$ be the dual functions of $\{\widetilde{N}_\alpha\}$ in $\mathrm{span}\{\widetilde{N}_\alpha\} \subset L^2(]0,1[)$. That is, $\{\widetilde{N}^*_\alpha\}$ satisfy the equations $\langle \widetilde{N}^*_\alpha, \widetilde{N}_\beta \rangle = \delta_{\alpha,\beta}$, where $\langle \cdot, \cdot \rangle$ is the standard $L^2(]0,1[)$-inner product. Taking the inner product of (A1) with $\widetilde{N}^*_\alpha$ we obtain the equality

$$c_\alpha = \left\langle \widetilde{N}^*_\alpha, \mathbf{r} \cdot \dot{\mathbf{r}} \right\rangle = \sum_{i,j} \mathbf{d}_i \cdot \mathbf{d}_j \left\langle \widetilde{N}^*_\alpha, N_i \dot{N}_j \right\rangle. \tag{A2}$$

Equation (A2) implies that c_α are quadratic forms of the vector of control variables $\mathbf{d}$. Naturally we arrive at the following optimization problem

$$\min_{\mathbf{d}} \max_{\alpha} |c_\alpha|, \tag{A3}$$

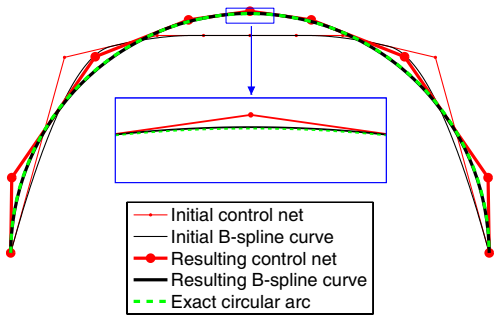

Figure A1. Approximation of the circular arc $x^2 + y^2 = 4^2$, $y \geq 0$ by a quadratic B-spline curve with the knot vector $\boldsymbol{\Xi} = \{0, 0, 0, 1/5, 2/5, 7/15, 8/15, 3/5, 4/5, 1, 1, 1\}$, using the optimization problem (A3). The B-spline curve is used as the truncation boundary in the model in Fig. 2.

which can be numerically solved to approximate stationarity using the same approach as the optimization problem (10). Utilizing (A3), we obtain a good approximation for the circular truncation boundary, see Fig. A1.

REFERENCES

1. Ding, Y., "Shape optimization of structures: A literature survey," *Computers & Structures*, Vol. 24, No. 6, 985–1004, 1986.
2. Delfour, M. and J. Zolésio, *Shapes and Geometries. Analysis, Differential Calculus, and Optimization, Advances in Design and Control*, Vol. 4, Society for Industrial and Applied Mathematics (SIAM), Philadelphia, PA, 2001.
3. Mohammadi, B. and O. Pironneau, *Applied Shape Optimization for Fluids.*, Oxford University Press, 2001.
4. Braibant, V. and C. Fleury, "Shape optimal design using B-splines," *Comput. Methods Appl. Mech. Engrg.*, Vol. 44, No. 3, 247–267, 1984.
5. Olhoff, N., M. P. Bendsøe, and J. Rasmussen, "CAD-integrated structural topology and design optimization," *Shape and Layout Optimization of Structural Systems and Optimality Criteria Methods, CISM Courses and Lectures*, Vol. 325, 171–197, Springer, Vienna, 1992.
6. Nguyen, D. M., A. Evgrafov, A. R. Gersborg, and J. Gravesen, "Isogeometric shape optimization of vibrating membranes," *Comput. Methods Appl. Mech. Engrg.*, Vol. 200, Nos. 13–16, 1343–1353, 2011.
7. Hughes, T., J. Cottrell, and Y. Bazilevs, "Isogeometric analysis: CAD, finite elements, NURBS, exact geometry and mesh refinement," *Comput. Methods Appl. Mech. Engrg.*, Vol. 194, Nos. 39–41, 4135–4195, 2005.
8. Wall, W., M. Frenzel, and C. Cyron, "Isogeometric structural shape optimization," *Comput. Methods Appl. Mech. Engrg.*, Vol. 197, Nos. 33–40, 2976–2988, 2008.
9. Cho, S. and S. H. Ha, "Isogeometric shape design optimization: Exact geometry and enhanced sensitivity," *Struct. Multidiscip. Optim.*, Vol. 38, No. 1, 53–70, 2009.
10. Nagy, A., M. Abdalla, and Z. Gurdal, "Isogeometric sizing and shape optimisation of beam structures," *Comput. Methods Appl. Mech. Engrg.*, Vol. 199, Nos. 17–20, 1216–1230, 2010.
11. Qian, X., "Full analytical sensitivities in nurbs based isogeometric

shape optimization," *Comput. Methods Appl. Mech. Engrg.*, Vol. 199, Nos. 29–32, 2059–2071, 2010.

12. Seo, Y. D., H. J. Kim, and S. K. Youn, "Shape optimization and its extension to topological design based on isogeometric analysis," *International Journal of Solids and Structures*, Vol. 47, Nos. 11–12, 1618–1640, 2010.
13. Cottrell, J. A., Y. Bazilevs, and T. J. R. Hughes, *Isogeometric Analysis: Toward Integration of CAD and FEA*, J. Wiley, West Sussex, 2009.
14. Knupp, P. and S. Steinberg, *Fundamentals of Grid Generation*, CRC Press, Boca Ranton, 1993.
15. Gravesen, J., A. Evgrafov, A. R. Gersborg, D. M. Nguyen, and P. N. Nielsen, "Isogeometric analysis and shape optimisation," *Proceedings of NSCM-23: The 23rd Nordic Seminar on Computational Mechanics*, Vol. 23, 14–17, 2010.
16. Aage, N., N. Mortensen, and O. Sigmund, "Topology optimization of metallic devices for microwave applications," *International Journal for Numerical Methods in Engineering*, Vol. 83, No. 2, 228–248, 2010.
17. Allaire, G., "Conception optimale de structures," *Mathématiques et Applications*, Vol. 58, Springer, 2007.
18. Bendsøe, M. and O. Sigmund, *Topology Optimization. Theory, Methods and Applications*, Springer-Verlag, Berlin, 2003.
19. Jin, J., *The Finite Element Method in Electromagnetics*, John Wiley & Sons, New York, 2002.
20. Adams, R., *Sobolev Spaces. Pure and Applied Mathematics*, Vol. 65, Academic Press, New York, London, 1975.
21. Zienkiewicz, O. and R. Taylor, *The Finite Element Method, Vol. 1, The Basis*, 5th Edition, Butterworth-Heinemann, Oxford, 2000.
22. Gravesen, J., *Differential Geometry and Design of Shape and Motion*, Department of Mathematics, Technical University of Denmark, 2002, URL: http://www2.mat.dtu.dk/people/J.Gravesen/cagd.pdf.
23. Piegl, L. and W. Tiller, *The NURBS Book (Monographs in Visual Communication)*, Springer-Verlag, Berlin, 1995.
24. De Boor, C. and G. Fix, "Spline approximation by quasiinterpolants," *J. Approximation Theory*, Vol. 8, 19–45, 1973.
25. MathWorks Inc., URL: http://www.mathworks.com.
26. Abramowitz, M. and I. A. Stegun, *Handbook of Mathematical Functions with Formulas, Graphs, and Mathematical Tables*, Dover, New York, 1964.

27. Balanis, C. A., *Advanced Engineering Electromagnetics*, Wiley, New York, 2005.
28. COMSOL Inc., URL: http://www.comsol.com.
29. Cheng, D. K., *Fundamentals of Engineering Electromagnetics*, Addison-Wesley, Reading, Massachusetts, 1993.
30. Aage, N., *Personal Communication*, 2011.